LAWRENCE
LIVERMORE
NATIONAL
LABORATORY

UCRL-TR-201115

Status Report on High Explosive and Laser Driven Al6061-T651

J.M. McNaney, J.E. Edwards, R. Becker, K.T. Lorenz, B. Remington

November 14, 2003

This work was performed under the auspices of the U.S. Department of Energy by University of California, Lawrence Livermore National Laboratory under Contract W-7405-Eng-48.

Status Report on high explosive and laser driven Al6061-T651

J.M. McNaney, J.E. Edwards, R. Becker, T. Lorenz, B. Remington

This report describes work done using isentropic drives based on high-explosives and lasers, along with recovery and ex-situ examination, to characterize material deformation behavior.

Baseline Material Characterization

The material considered is a commercial aluminum alloy, 6061 in the T651 peak aged condition. It was supplied in the form of a 52 mm diameter bar from stock given to V.A. Raevsky (Agreement No. B512964) in order to investigate high explosive (HE) shocklessly driven Raleigh-Taylor growth experiments. A number of characterization techniques were used to investigate the material including standard metallography, electron backscatter diffraction (EBSD), and microhardness.

Metallography of the as-received material, viewed in the plane perpendicular to the axis of the rod, revealed two distinct regions: one characterized by uncharacteristically large grains (500-1600 μm) and one with a more common grain structure (fig. 1) consisting of grains approximately 20-50 μm in diameter. Grains in both of these regions were elongated in the drawing direction (parallel to the rod axis). These regions were separated by a transition region consisting of partially recrystallized large grains with a large number of subgrain boundaries. These observations indicate that the bar has been partially recrystallized during the manufacturing process. EBSD measurements indicated the presence of a marked texture in both regions as shown in the pole figures of Figure 1.

Microhardness measurements showed no discernable difference in these two regions indicating the mechanical properties are roughly the same. This is not surprising since the alloy derives its strength from precipitation with a negligible contribution from grain boundary hardening.

Experiments

High pressure, high strain rate materials deformation experiments were carried out on two experimental platforms, both producing quasi-isentropic shockless compressive (ICE) loading; a high explosive drive [1] and a laser-based drive [2]. Each platform provided a recovery capability for post-test material characterization. In the case of the HE driven tests, momentum trapping was used while dissipation in relatively thick samples was used in the short-pulse laser-based experiments. All samples were loaded parallel to the axis of the aluminum bar.

Hydrodynamic Modeling

The laser experiment was modeled with the Arbitrary Lagrangian Eulerian (ALE) hydrocode CALE [7]. The calculations included a laser deposition model to capture the laser-reservoir interaction, and a Steinberg-Guinan strength prescription together with realistic equations of state to simulate the cratering process. The 2-D axisymmetric

calculations provide detailed information on the loading pulse as it traverses the sample, as well as the overall deformation field. The material was considered to be isotropic with a simple Steinburg-Guinan type constitutive response. While the stress on the front face of the sample is constrained by the boundary conditions to follow the incident pressure pulse, as discussed above, the pressure wave steepens as it travels through the material and eventually becomes a shock. This is demonstrated for the drives considered here in figure 2, where two indications of the shockless/shock transition are shown. One indication lies in the slope of the loading versus depth curve, which displays a definite step in the case of shock loading, while another can be seen in the rise in temperature as the material is compressed, which is relatively higher for the shock loaded region. For the drives used in this study, the region of shocklessly deformed material is limited to ≈100 μm in the case of the 18 GPa drive and ≈ 50 μm in the case of the 38 GPa drive.

HE platform tests

A brief description of the experimental methods used is given below while a comprehensive report may be found in [1]. Following the method of [1], quasi-isentropic loading is produced using a two-stage high explosive drive schematically shown in figure 3. A plane wave detonation in the first stage accelerates an impactor, which detonates the second stage in the over-compressed detonation regime. Explosion products expanding into a gap provides smooth loading of the facing material. Recovery of samples was enabled through the use of a momentum trapping arrangement (figure 3). Two experiments were performed with peak pressures of 12 and 38 GPa (figure 4). Samples were ≈ 25 mm diameter, 40 mm thick for the 12 GPa drive and ≈ 30 mm diameter, 10 mm thick for the 38 GPa drive. As can be seen, the higher pressure sample was partially shocked even at a relatively shallow depth. Strain rates, operationally defined as $(d\rho/dt)/3\rho$ where ρ is the material density, were in the range ~10^5/s at the loading surface and increased as the loading wave traversed the sample. Additionally, this sample appeared to contain a spall plane indicating a tensile reflection and incomplete momentum trapping. As such no characterization of this sample was performed.

Laser platform tests

A laser-based shockless drive, recently developed by [2], was used to load the samples, which were 3 mm in diameter and 3 mm thick. A schematic of the experimental setup is shown in figure 5. A strong shock is generated by direct laser ablation of an aluminum coated (100 nm) polycarbonate reservoir ($\rho \approx 1.2$ g/cm^3, 170 μm thick) using a 3.7 ns square pulse with an intensity of ≈ $5\text{x}10^{12} – 10^{13}$ W/cm^2. Upon reaching the rear of the reservoir the plasma expands across a gap, separating the reservoir from the sample, producing a smooth, quasi-isentropic loading. Experiments were carried out at two peak pressures, 18 and 38 GPa to correspond with the HE based experiments, as shown in figure 6. Strain rates were ~ 5×10^6/s and ~ 5×10^7/s for the 18 and 38 GPa drives respectively. A total of 4 samples were recovered, one at each pressure for the small and large grained material previously described.

Results

Due to the difficulty and expense of characterizing the small-grained regions, only large grained material was characterized. This allowed observation of the coarse slip band (CSB) structures noted in [1] using standard metallographic analysis. EBSD of sectioned HE and laser driven samples was done in a limited number of cases to ascertain the nature of the slip bands. The EBSD results were inconclusive and are not presented here.

HE platform tests

Material recovered from HE experiment was provided sectioned parallel to the drive direction along the sample centerline. Recovered samples were found to have sustained a permanent shape change corresponding to a uniaxial compressive strain of about 30%. Standard metallographic characterization was performed after polishing and etching to reveal the material microstructure. No shear bands were seen in the sample. However, the presence of coarse slip bands throughout the sample was noted (Figure 7).

It has been suggested [1] that the fraction of grains containing these CSBs and their spacing is proportional to the strain rate during loading. To this end an analysis of the frequency of grains observed to have CSBs as a function of depth into the sample (strain rate) was carried out. As shown in Figure 8, we find no statistically significant change in the fraction of grains containing CSBs as a function of depth into the sample. This may not be surprising since recent work [4] has identified the peak shock pressure as the most important variable in determining subsequent material microstructure and deformation behavior.

Laser platform tests

Samples were recovered at both 18 and 38 GPa corresponding to peak pressures attained during loading on the HE-based platform. An overview of the recovered and sectioned samples is shown in figure 9. The most obvious feature is the presence of a crater. As should be expected, the residual crater is deeper for the higher applied pressure. In contrast to the samples loaded on the HE platform, the overall shape of the laser driven samples is changed only in the region of the crater.

In the sample loaded to 38 GPa, there appears to be a line of voids ***parallel*** to the direction of propagation of the compression wave and noticeably off the centerline of the sample, a location that is not supported by the overall symmetry of the sample and test. A closer look (Fig. 10) reveals that this feature occurs along the grain boundary and indicates that these boundaries are potential “weak” locations in the microstructure. Additional experiments and calculations are necessary to understand the sequence of events, which led to the formation of this feature.

In contrast to samples recovered from the HE loading, no CSBs were observed in the 18 GPa laser loaded samples while some evidence of CSBs were found in the sample loaded to 38 GPa (Fig. 11). There are a number possible explanations for the

observations regarding the CSBs. In the 18 GPa sample, it may be that the decaying pressure wave limited the volume of material subjected to conditions necessary to form CSBs. However, it seems unlikely that this explanation would account for the observations in the 38 GPa sample. In this higher pressure sample, the load would have remained well above the level (of 12 GPa) known to cause CSB formation in HE driven samples. It does seem possible that an insufficient number of grains were available to ensure observation of CSBs given that only about 10% of grains were observed, by metallographic techniques, to contain these structures. In the 38 GPa sample, where ≈20-30 grains experienced pressures in excess of 12 GPa produced only partial CSBs in a single grain, this reasoning does not seem to explain the observations. An alternate explanation is that the gradient in pressure, wherein the plastic strain accumulates, is too steep to support the formation and propagation of the CSBs. This explanation is related to the discussion, below, on formation of even larger slip based structures, namely shear bands. However, considerable additional work would be required to investigate these issues.

Crystal plasticity

To investigate the effects of material texture and assess the extent to which shear band formation was likely, a crystal plasticity based model was implemented into the computer code ALE3D [5]. This implementation is based on the framework outlined in Peirce, et al. [6] but modified for an iterative solution of the slip rates. Deformation by crystal slip is isochoric and decoupled from the pressure-volume response. The pressure was calculated using the same Mie-Gruneisen equation of state as in the CALE simulations described above. This simple modification permits sharpening of the pressure gradient into a shock. Although this version of the model does not provide for pressure dependence of the slip system constitutive response or shear moduli, it is expected that it will capture the essential features of both the shock development and deformation by crystallographic slip.

These calculations were carried out using the small-grained material as it was expected that the high degree of texture present in this material might lead to strong crystallographic effects. It should be emphasized that the model employed here looks at shear bands formed through geometric softening. No thermal softening or heterogeneous localization phenomena are considered. As such, the conditions for formation of shear bands identified from this type of calculation would represent some upper bound condition. Results from calculations, based on the small-grained material, are presented in figure 12. It can be seen that the crystallographic texture in this material results in some preferential accumulation of plastic strain in grains oriented for “easy” slip with respect to the drive direction. However, these localized regions do not result in the formation of shear bands. An explanation for this behavior may be seen by considering the stress and strain gradients present during the experiment. These are presented in figure 13 when the incident pressure is at its peak. While only the loading portion is shown, the strain is accumulated during both loading and unloading. In each case, the deformation accumulates over a distance of less than ≈50 μm in the wave propagation direction resulting in a strain gradient on the order of 10^4/m. Further

propagation of the wave into the material only serves to concentrate the accumulation of strain over an ever smaller region as it steepens into a shock. The limited spatial scale over which plastic flow occurs hinders or prevents the formation shear bands which must form in deformation fields with much larger overall length scales, presumably spanning many grains. This implies that formation of shear bands using the high strain rate laser-based drives is less likely to produce the kind shear banding often observed in gas gun and high explosive driven material. Note that these limitations are a consequence of the relative sizes of the grains and the pressure gradient. Were a material with sufficiently small grains used, it should be possible to produce shear bands using the laser-based drive although their physical size would be limited.

Strength from topography (laser-driven samples)

The presence of a crater on the drive surface implies significant local deformation has taken place. Calculations, described above, indicate the crater depth is a strong function of the loading pulse peak pressure and the calculated depths show good agreement with crater depths measured from recovered samples (figure 14). This is true of both the large and small grained material. This agreement suggests that the simple constitutive models employed are able to capture the basic deformation behavior under these high pressure, high strain rate conditions. Perhaps this is not surprising given that the region of material experiencing shockless loading is relatively small. As such, the deformation would be expected to occur under similar conditions as in the shock loaded strength tests used to provide data for the constitutive models. Despite the high degree of crystallographic texture present in the starting material, no obvious effect was observed. This may be due to the multiplicity of slip systems available in aluminum which would be expected to somewhat ameliorate the orientation effects.

One major difference between shock and shocklessly driven material is the expectation that thermal softening should affect the deformation behavior. At the lower drive pressure (18 GPa) the temperature rise during shockless (isentropic) loading is not appreciably different than that accompanying shock loading conditions (fig. 2) and little difference in the thermal softening behavior is expected. This is in contrast to the marked rise in temperature that accompanies shock loading at the higher pressure (38 GPa) as compared to shockless loading.

In the current geometry the formation of the crater occurs over a volume that is large compared to the shocklessly driven region. For example, for the 18 GPa drive, the crater depth is ~150 μm, (see Fig. 9a) which is approximately the same as the extent of the region that experienced the shockless loading (Fig. 2a) while in the case of the 38 GPa drive, the crater depth is ~300 μm, whereas the extent of material subjected to shockless loading is only ~50 μm. In both cases the crater diameter is ~1000 μm and it is this size that sets the scale for volume of material involved in crater formation. This implies that the overall deformation of the sample, such as the cater depth and shape, is dominated by the shock-loaded material. However, in all cases the local material behavior would be expected to depend on the local (shockless or shocked) loading conditions. As such, only observation of the material behavior on a local scale would be likely to discern differences between the shock and shockless drive

It should be noted that in contrast to the laser-driven experiments performed here on bulk samples, other geometries should be considerably more influenced by the shockless drive employed. This would be especially true for very thin samples, such as those employed in strength measurements using Raleigh-Taylor instability [8]. In this type of geometry the entire sample is subjected to nearly isentropic loading conditions and, for a given peak pressure, both the associated temperature rise and the accompanying strain rate are considerably lower than that of shock loaded material. This is particularly true at high pressures where any differences in deformation behavior between shock and shocklessly driven material would be apparent.

References

[1] V. A. Raevsky, report for Task I under Agreement No. B512964

[2] J. Edwards, T. Lorenz, et. al., submitted to PRL, April 2003

[3] J.F. Barnes et al, J. App. Phys. **45**(2), 727,(1974)

[4] R.T. Gray III, Submitted to Met. Trans., April 2003.

[5] Dube, E., Neely, R., Nichols, A., Sharp, R., and Couch, R., 2001. Users Manual for ALE3D-An arbitrary Lagrange / Eulerian 3-D Code System, Lawrence Livermore National Laboratory.

[6] Peirce, D., Asaro, R.J. and Needleman, A., Acta Metallurgica, vol.30, no.6, June 1982, pp.1087-119.

[7] Users Manual for CALE, Lawrence Livermore National Laboratory.

[8] D.H. Kalantar, et. al., Phys. Plasmas, **7**, 1999 (2000).

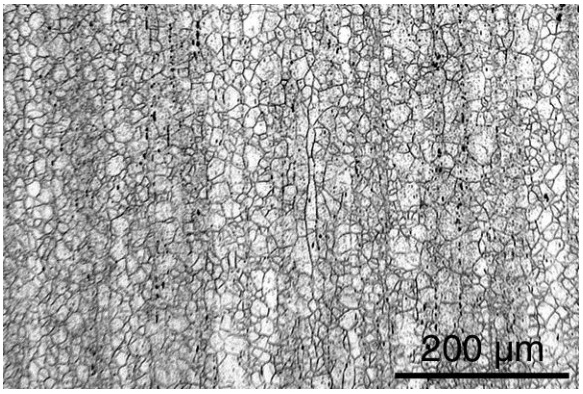

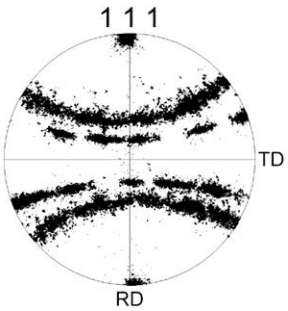

(a)

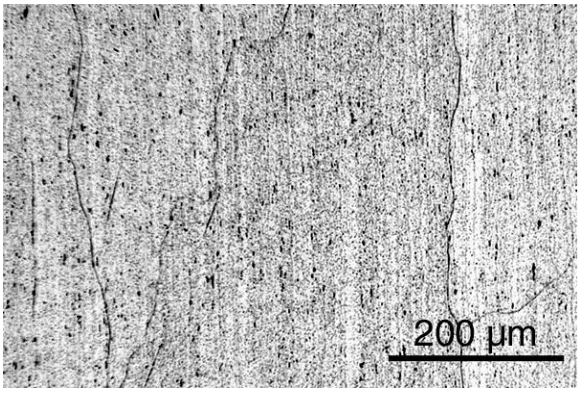

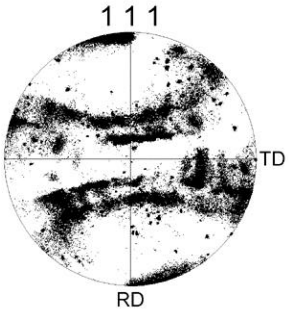

(b)

Figure 1: Metallography and associated pole figues for Al6061-T6 material used in this study showing (a) fine grained region and (b) coarse grained region viewed along the axis of the extrusion.

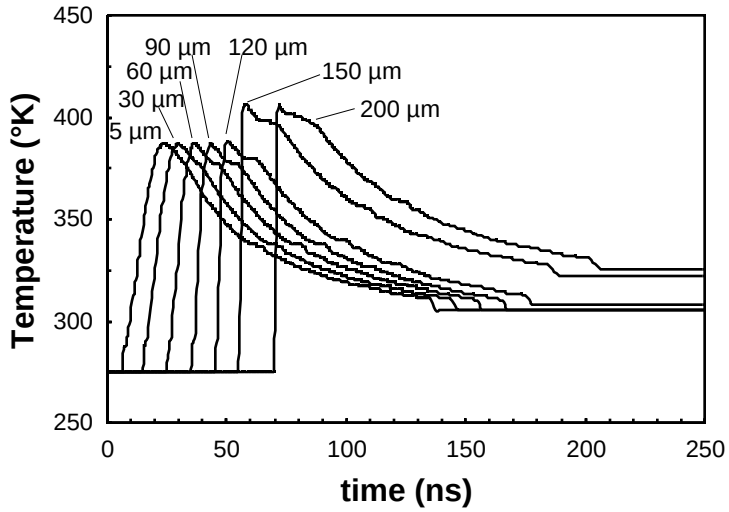

(a)

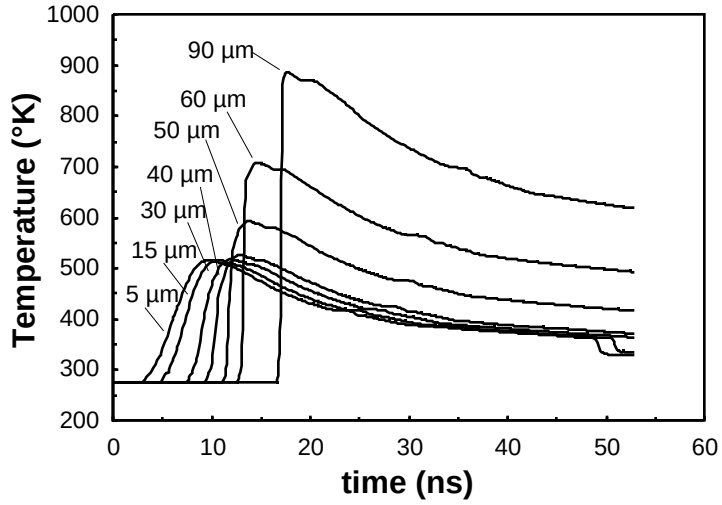

(b)

Figure 2. Transition from isentropic to shock conditions as indicated by temperature change. The temporal variation of temperature at various depths (labeled) shows increased temperature, at the same peak pressure, under shock conditions for the (a) 18 GPa and (b) 40 GPa drives.

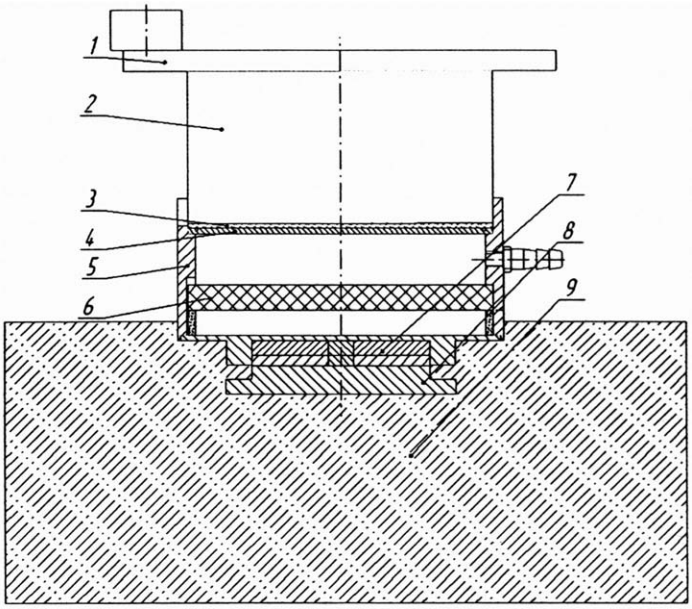

1. Flat shockwave generator
2. First stage HE
3. Damper
4. Steel impactor
5. Sealing cylinder
6. Second stage HE
7. Target assembly
8. Aluminum plate
9. Concrete

(a)

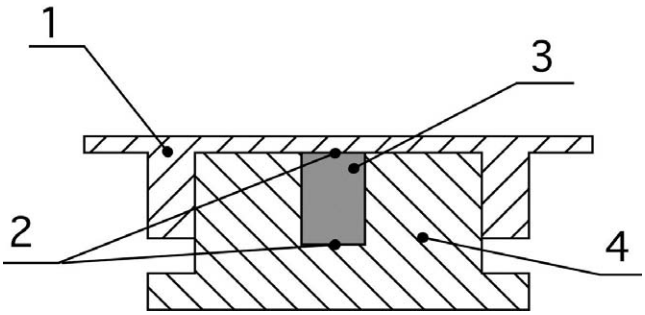

1. Protective Al screen
2. Manganin pressure pins
3. Sample
4. Al momentum trap

(b)

Figure 3. (a) Overall experimental setup for 2-stage isentropic HE drive with (b) detail of momentum trapping arrangement.

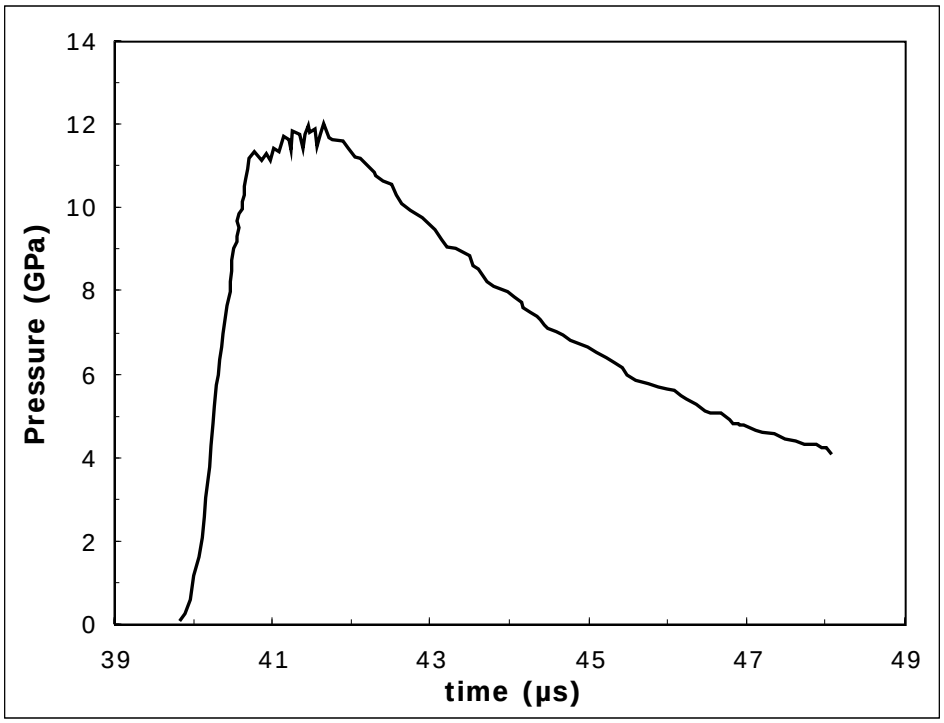

(a)

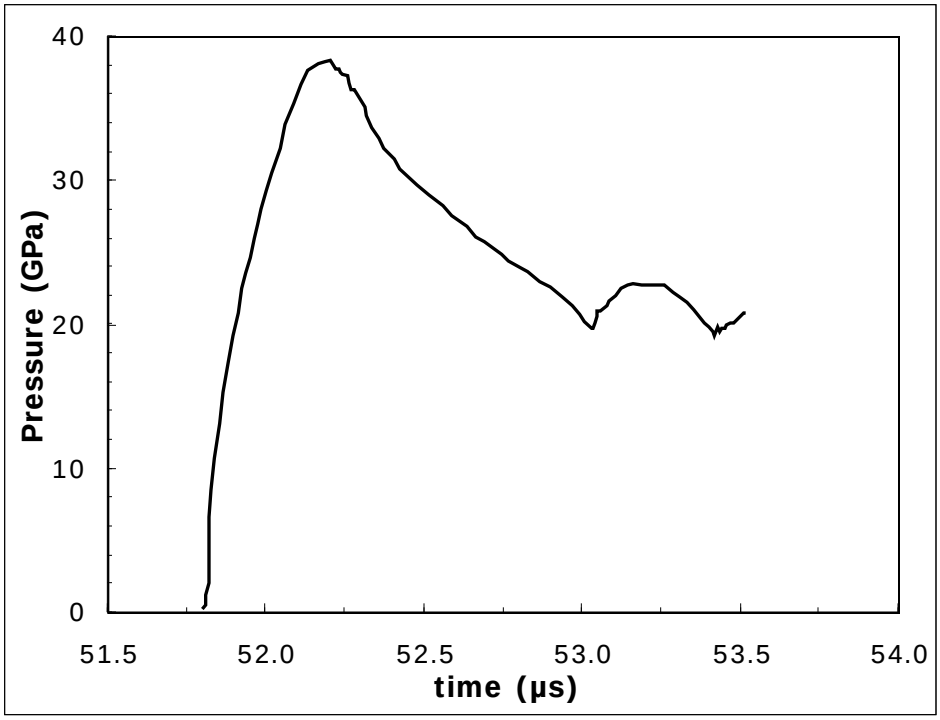

(b)

Figure 4. Pressure versus time near the loading surface for the (a) 12 GPa and (b) 40 GPa HE drives.

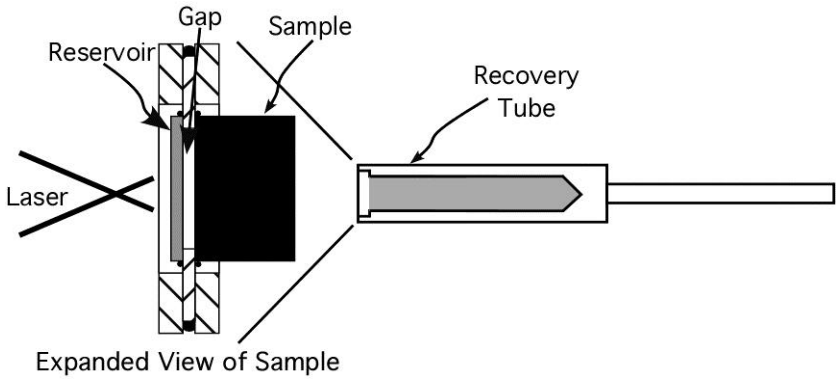

Figure 5. Schematic of recovery apparatus with exploded view of ICE drive.

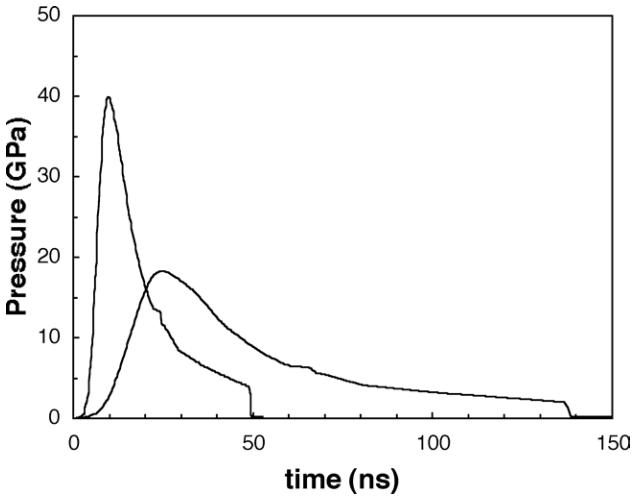

Figure 6. Calculated drive surface pressure versus time profiles for laser experiments conducted in this study.

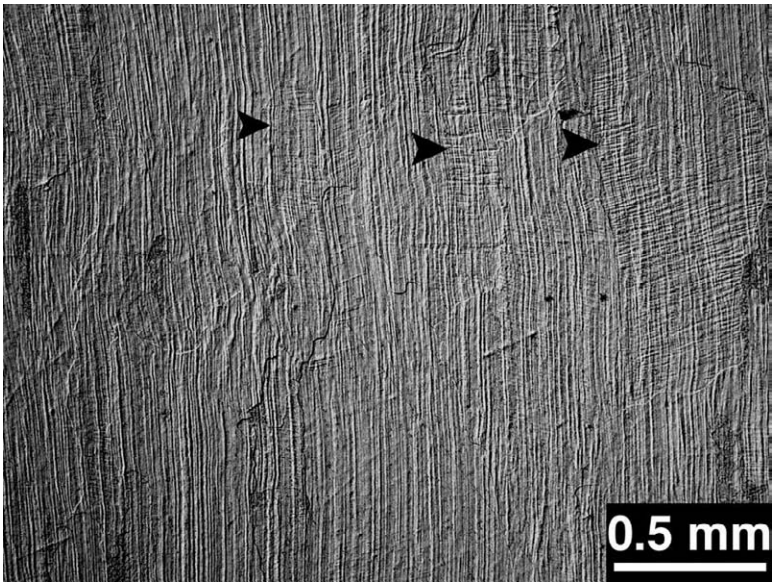

Figure 7: Cross section of HE sample loaded to 12 GPa and recovered. Coarse slip bands, indicated by arrows, are present throughout the sample though most grains appear to have none. Loading direction proceeded from top to bottom of photo. Note that the vertical bands coincide with the extrusion direction of the original material.

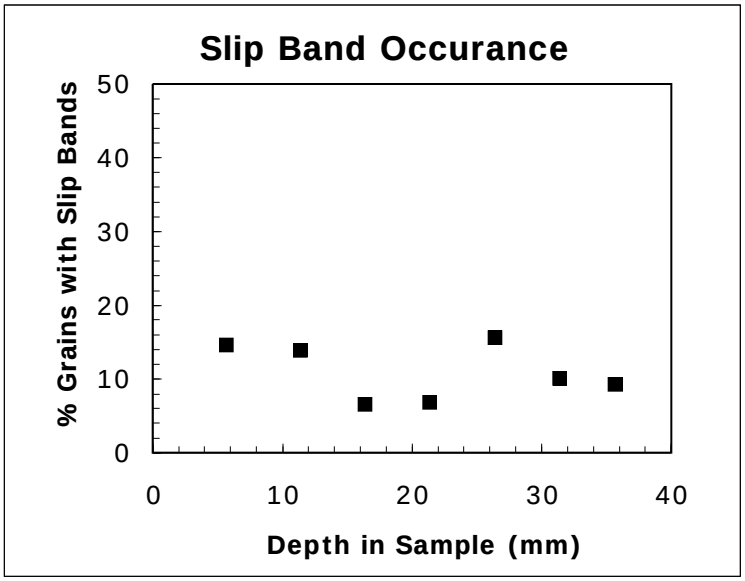

Figure 8: Observation of grains containing coarse slip bands as a function of distance into the sample (referenced to initial sample geometry) showing no systematic increase with strain rate (depth).

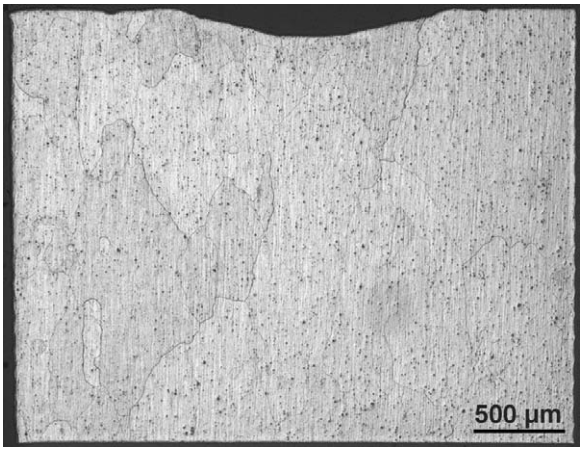

(a)

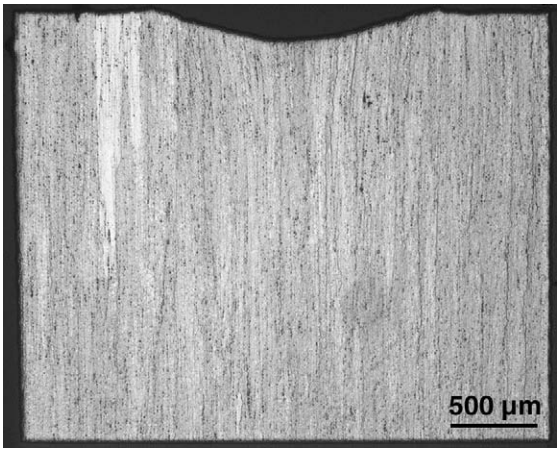

(b)

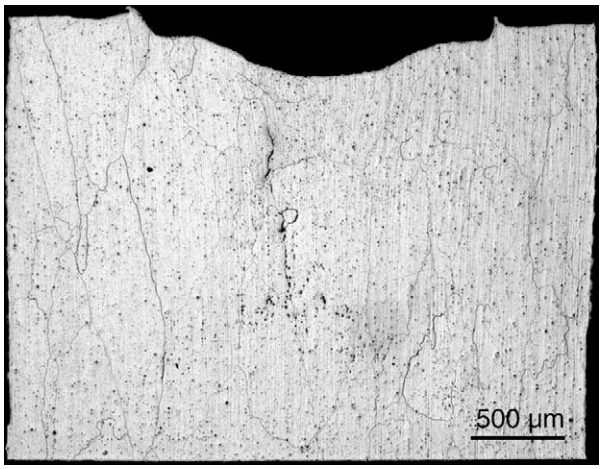

(c)

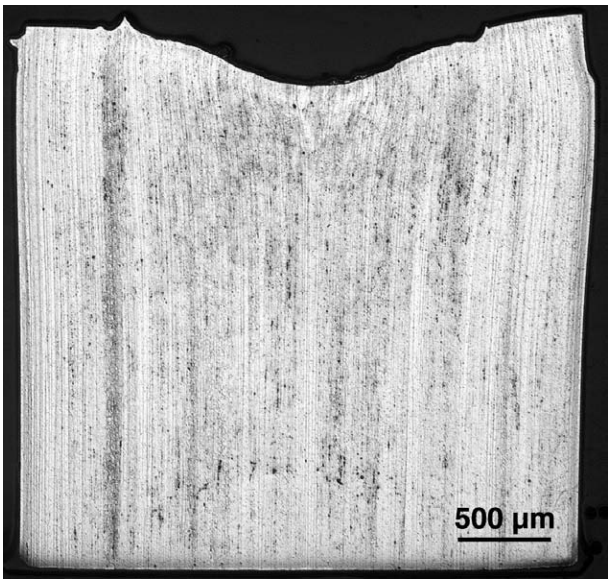

(d)

Figure 9: Overview of samples recovered from laser-based platform after peak pressure of 18 GPa for (a) large grained and (b) small grained material and 38 GPa for (c) large grained and (d) small grained material.

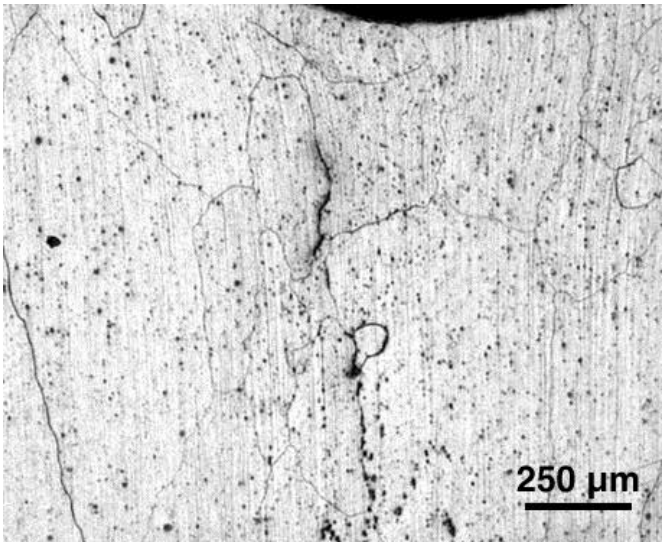

Figure 10: Line of voids parallel to drive direction. Note how void plane follows grain boundaries which are also parallel to the drive direction and slightly off the centerline.

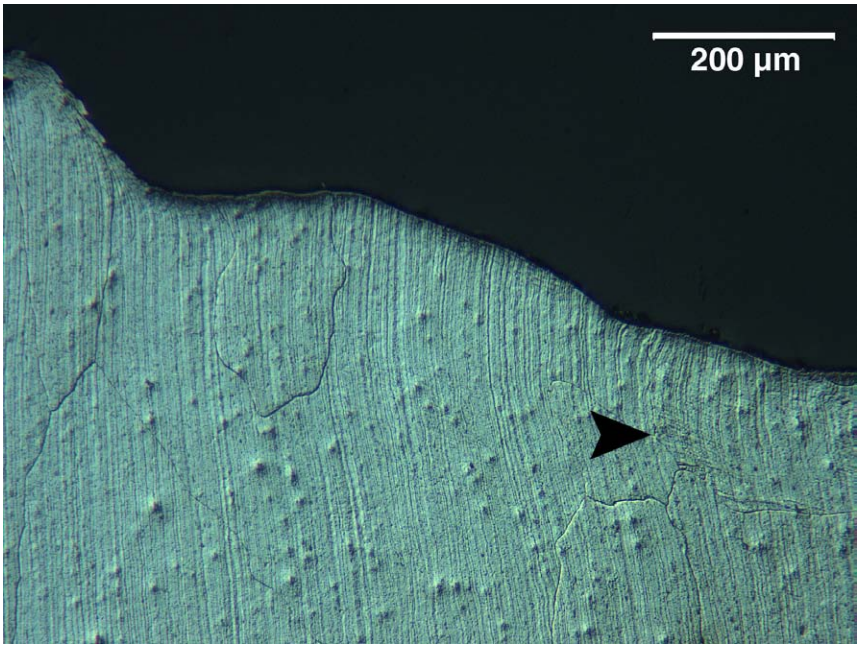

Figure 11: Evidence of coarse slip bands (denoted by arrow) in the sample loaded to 38 GPa.

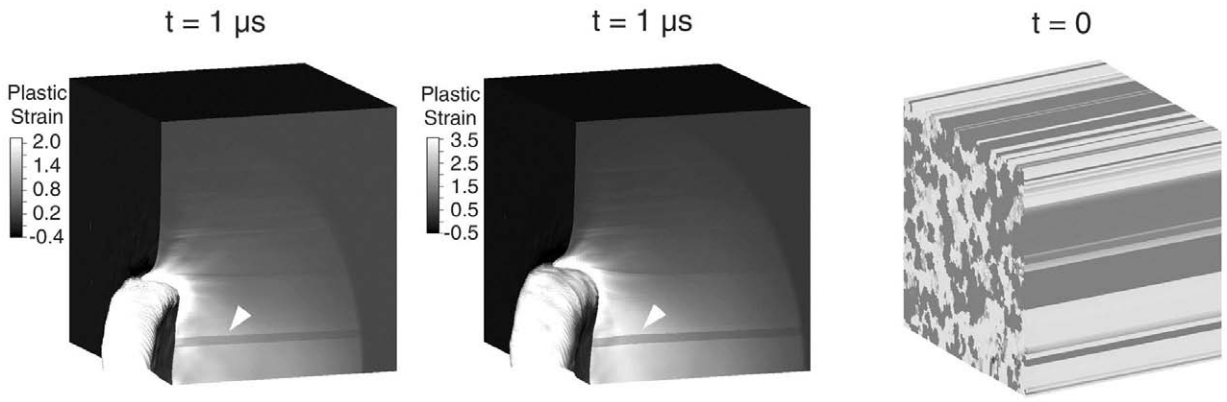

(a) **(b)** **(c)**

Figure 12: Results from crystal plasticity simulations of laser-driven samples showing total plastic strain after peak pressure of (a) 18 GPa and (b) 40 GPa (due to symmetry, only one quarter of the mesh is shown). The crater is the depressed region at one corner and the arrows indicate localized deformation in “easy slip” grains. The initial microstructure for crystal plasticity based calculations (grain orientation is indicated by gray level) is shown in (c).

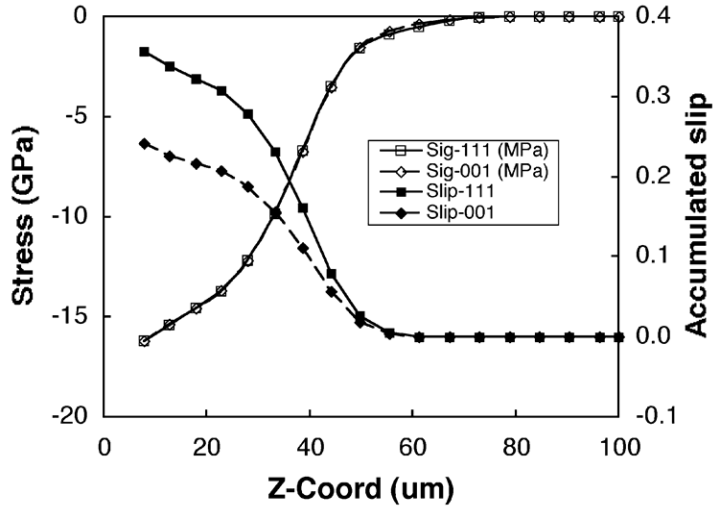

(a)

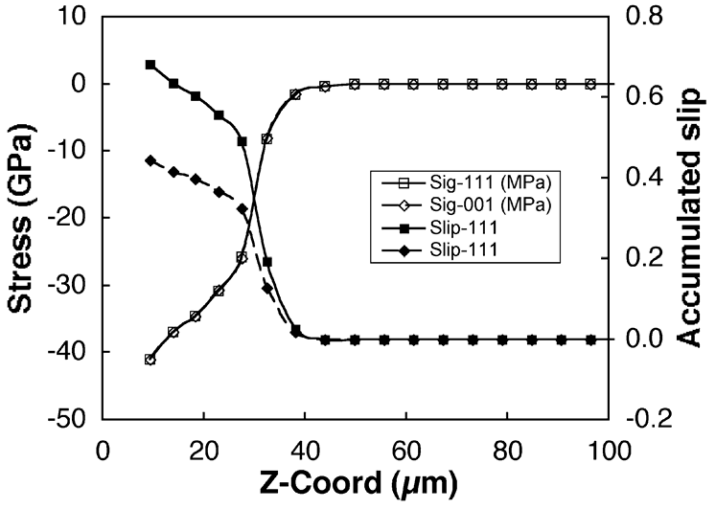

(b)

Figure 13. Results from crystal plasticity simulations of the (a) 18 GPa and (b) 40 GPa drives showing stress (open symbols) and strain (closed symbols) as a function of distance from the drive surface for two different grain orientations. Note that the strain accumulation occurs over ≈ 20-40 μm which is on the order of the grain size.

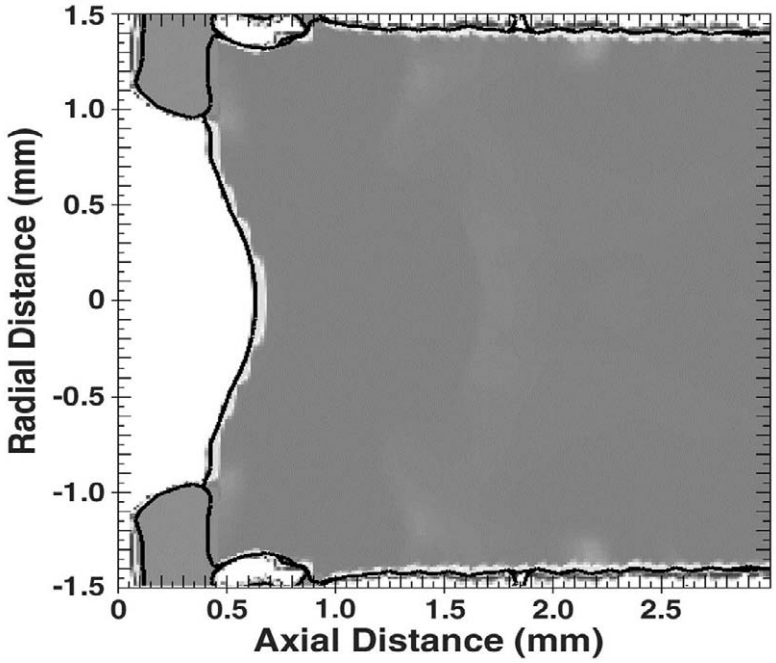

(a)

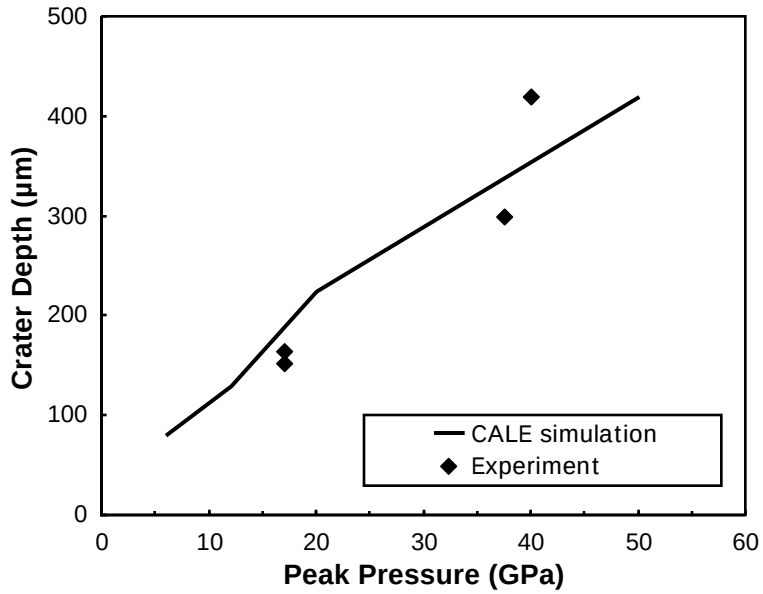

(b)

Figure 14: (a) Results of representative numerical calculation showing deformation resulting from 12 GPa drive. . (b) Experimental versus calculated crater depth. Good agreement indicates simple Steinburg-Guinan strength model describes the behavior of the Al6061-T6 used in this study